ACSNANO
www.acsnano.org
ARTICLE

Downloaded via XI'AN JIAOTONG UNIV on April 3, 2019 at 12:58:08 (UTC).
See https://pubs.acs.org/sharingguidelines for options on how to legitimately share published articles.

Low-Temperature Fusible Silver Micro/Nanodendrites-Based Electrically Conductive Composites for Next-Generation Printed Fuse-Links

Rui Yang, Yang Wang, Dang Wu, Yubin Deng, Yingying Luo, Xiaoya Cui, Xuanyu Wang, Zhixue Shu, and Cheng Yang*

Division of Energy and Environment, Graduate School at Shenzhen, Tsinghua University, Shenzhen 518055, People's Republic of China

Supporting Information

ABSTRACT: **We systematically investigate the long-neglected low-temperature fusing behavior of silver micro/nanodendrites and demonstrate the feasibility of employing this intriguing property for the printed electronics application, *i.e.*, printed fuse-links. Fuse-links have experienced insignificant changes since they were invented in the 1890s. By introducing silver micro/nanodendrites-based electrically conductive composites (ECCs) as a printed fusible element, coupled with the state-of-the-art printed electronics technology, key performance characteristics of a fuse-link are dramatically improved as compared with the commercially available counterparts, including an expedient fabrication process, lower available rated current (40% of the minimum value of Littelfuse 467 series fuses), shorter response time (only 3.35% of the Littelfuse 2920L030 at 1.5 times of the rated current), milder surface temperature rise (16.89 °C lower than FGMB) and voltage drop (only 24.26% of FGMB) in normal operations, easier to mass produce, and more flexible in product design. This technology may inspire the development of future printed electronic components.**

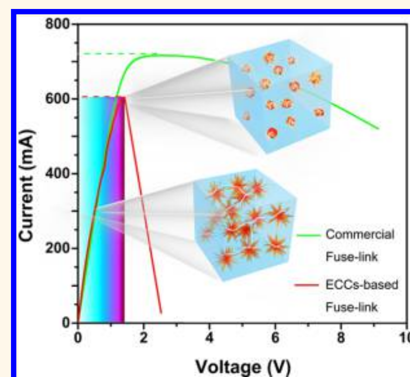

KEYWORDS: *silver micro/nanodendrites, electrically conductive composite, low-temperature fusing, printed electronics, fuse-link*

The last few decades have witnessed an explosive development of nanotechnology.[1−4] As materials' sizes are reduced to the nanoscale, their surface energy increases drastically, and thus they can sinter at lower temperatures. Joining nanosized metals and forming permanent metallurgical connections under a low processing temperature can significantly improve electrical and thermal interconnection, which has been regarded as a basic technique for printed electronics and micro/nanodevice fabrications.[5] To date, low-temperature sintering among versatile metallic nanostructures with different dimensional characteristics has been achieved by direct heating or cold welding, including zero-dimensional (0-D) nanoclusters[6,7] and nanoparticles,[8−10] one-dimensional (1-D) nanowires[11−13] and nanotubes,[9,14] two-dimensional (2-D) nanoflakes[9] and nanoplates,[15] and three-dimensional (3-D) nanosponges,[16,17] nanoflowers,[18] and nanonetworks.[19] However, to our knowledge, the fuse-blowing phenomenon of metallic nanostructures due to excessive heat input has rarely been investigated, although it may find extensive applications in electronic devices, such as fuse-links, ultrafine wiring, and temperature sensors.

Printed electronic technology enables the large-scale and low-cost fabrications of electronic devices and systems, as well as fast prototyping; hence it provides superior pathways in developing cost-effective electronics applications in various fields.[20] To date, tremendous efforts have been made to develop printed thin-film transistors (TFTs),[20,21] radio frequency identification (RFID) tags,[22] light-emitting diodes (LEDs),[23] *etc.* However, some other electronic components, such as capacitors, inductors, and fuse-links, have been rarely explored in printing technology. For instance, as a very basic electronic component, fuse-links have found extensive applications in most electrical and electronic devices, and the global market value is expected to reach US $53.56 billion by 2022, increasing at a compound annual growth rate of 5.92%.[24] However, they have experienced insignificant technological and configurational changes since they were invented over a century ago. Future electronic systems featuring higher integration and

Received: February 10, 2017
Accepted: July 18, 2017
Published: July 18, 2017

 © 2017 American Chemical Society

DOI: 10.1021/acsnano.7b00935
ACS Nano 2017, 11, 7710−7718

lower power consumption levels urgently require fuse-links having smaller form factors and lower fusing currents. Conventional plug-in and surface-mounted device (SMD) type fuses have been suffering from a series of disadvantages including complicated manufacturing processes, high cost, large package size, high fusing current, and slow response speed, and thus they can hardly meet the needs of future highly integrated, low cost, and high-performance electronic devices.

Herein, we report a fuse-link technology combining both nanotechnology and electronic printing technique. We pay close attention to the low-temperature fusing phenomenon of metallic nanostructures by systematically studying the fusing process of silver micro/nanodendrites and demonstrating the feasibility and advantages of printed fuse-links using silver micro/nanodendrites-based electrically conductive composites (ECCs) as the fusible element, *via* a facile and scalable electronic printing technique. Silver micro/nanodendrites have the typical 3-D radial configuration and abundant nanosized surface structures, rather than some other available micro-nanoparticles with an anisotropic configuration (*e.g.*, nanowires and nanoflakes) and limited surface features.[25] The 3-D radial configuration of silver micro/nanodendrites can render isotropic conductivity when being dispersed in a resin matrix and processed by conventional printing methods, which is essential in many cases where vertical interconnections are required. With the above advantages, the ECC-based fuse-link can be fabricated by directly printing or dispensing a small volume of the ECC paste between two conductive pads and, thus, can be easily prepared in mass production. Therefore, the fabrication process can be more simple and efficient than the existing piece-by-piece wire bonding one for the commercially available counterparts. In addition, by adjusting the constituents and dimensions of the printed ECC and managing the printing parameters, we can conveniently modulate the performance characteristics of the fuse-link. In this paper, by combining the superior low-temperature fusing cutoff characteristic of silver micro/nanodendrites, we developed printable fuse-link, which shows a series of prominent performance characteristics, *e.g.*, small form factor, wide-range adjustable fusing current, rapid response speed, and excellent reliability. Besides, we have prototyped three kinds of fuses, which show a superior functionality to the commercially available counterparts. They are (i) the miniaturized wiring-type fuse-link (MWF), which has an ultralow fusing current and can cater to the future higher integration and lower dissipation circuits; (ii) the thin gasket-type fuse-link (TGF), which is aimed to provide safety issue solutions of lithium-ion batteries (LIBs), and (iii) the deformable and reworkable silicone grease-based fuse-link (SGF), which can be used in stretchable and self-healable electronic devices. These high-performance printed fuses, based on low-temperature fusible ECCs, show great potential in addressing some critical challenges in future electric and electronic protection and may shed light on the development of other isolated components.

RESULTS AND DISCUSSION

Working Mechanism of the Fuse-Link. Typically, a commercially available tube-type fuse-link mainly comprises a piece of low-melting-point metal or alloy wire mounted in glass or ceramic housings, which is sealed by metal terminals, as illustrated in Figure 1a. Below rated current, the fuse-link functions as a piece of conductive wire, whereas, once the current exceeds its rated value, the temperature rises rapidly to reach the melting point of the metal or alloy wire. Subsequently, the fuse-link melts and cuts off the circuit, and thus prevents the circuit from overheating or becoming overloaded, which is extremely prone to incur catastrophic failure.[26,27] This structural configuration has rarely been essentially altered since it was invented in the 1890s.

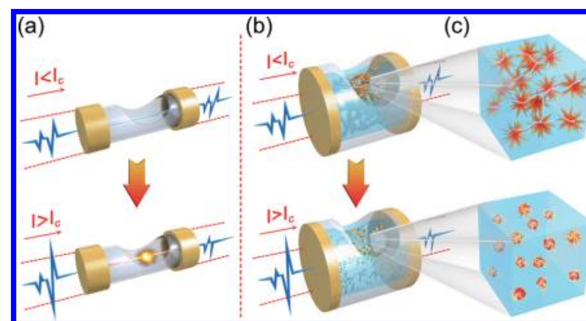

Figure 1. Schematic illustration of the commercial glass-tube fuse-link and the as-prepared ECC-based fuse-link. (a) A safe current ($I < I_c$) can flow through the glass-tube fuse, while an overloaded current ($I > I_c$) would be cut off *via* the melting of the metal wire. (b) Under normal operation ($I < I_c$), the current flows through the conductive network built by silver micro/nanodendrites; however, in the case of an overcurrent situation ($I > I_c$), the established conductive network collapsed to cut off the circuit. (c) Demonstration of the working mechanism of the ECC-based fuse-link.

Figure 1b schematically shows our superior design of fuse-links. The silver micro/nanodendrites-based ECC is used as the fuse element to replace traditional metal or alloy wires. Under normal operation conditions, a thermal equilibrium can be attained through the heat exchange process between the fuse element and the surrounding environment. However, once the applied current exceeds its rated current, the heat dissipation rate fails to keep pace with the heat production rate, and thus the surplus heat accumulates in the fuse element. The extra heat triggers the melting and shrinking of the outer nanosized rims and submicrosized branches of the silver micro/nanodendrites, leading to collapse of the previously established conductive network, as shown in Figure 1c. Hence, the electrical interconnection is interrupted promptly and opportunely to protect the core electronic components.

Low-Temperature Fusing Behavior of the Silver Micro/Nanodendrites. The as-prepared silver micro/nanodendrites have an average size of around 7 μm and possess three levels of branches with ample micro- and nanostructures (Figure 2a and Figure S1). This representative structural characteristic renders the silver micro/nanodendrites with a remarkable sintering ability at different temperature rising stages, as shown in Figure 2a–c and Figure S2. The fusing process of the silver micro/nanodendrites can be summarized as two stages: the first stage occurred at about 200 °C, when the limbic nanosized (tertiary branches) and submicrosized (secondary branches) structures melted and disappeared, and the melted structures coalesced with the primary branches, forming a shortened and thickened surface structure with an average branch diameter of about 1 μm (Figure 2b). In the second stage, as the temperature rose to 400 °C, the primary branches fused and shrank, leading to an irregular micro-structured particle with some incompletely disappeared pillar branches, as shown in Figure 2c. Meanwhile, the adjacent silver micro/nanodendrites fused with each other, indicating a low-

DOI: 10.1021/acsnano.7b00935
ACS Nano 2017, 11, 7710–7718

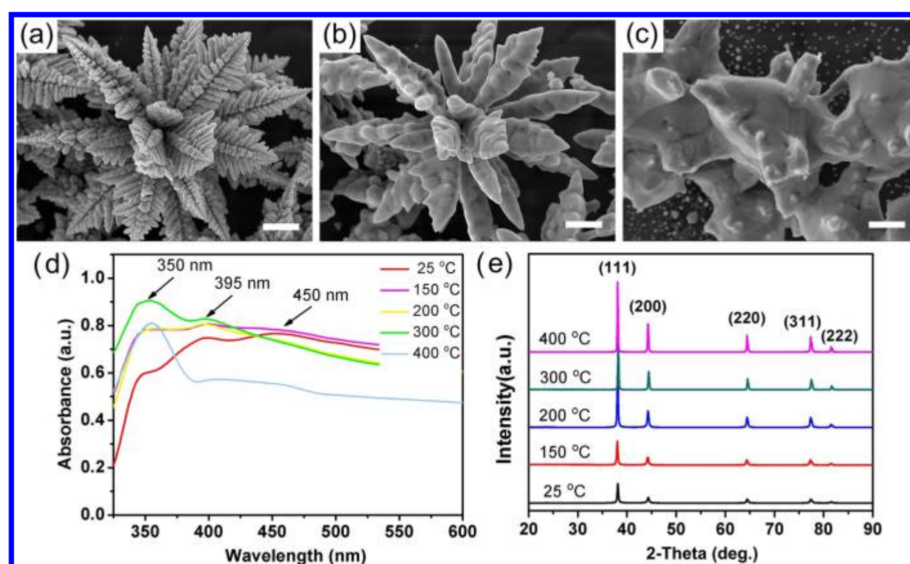

Figure 2. Fusing behavior of the silver micro/nanodendrites. (a−c) SEM images of the silver micro/nanodendrite after being annealed at different temperatures in a nitrogen atmosphere (all scale bars are 1 μm). (a) SEM image of the as-prepared silver micro/nanodendrite at room temperature. (b) SEM image of the silver micro/nanodendrite after being annealed at 200 °C. (c) SEM image of the silver micro/nanodendrite fusing together with adjacent ones, after being heated at 400 °C in a nitrogen atmosphere. (d) UV−vis absorption spectra (reflective mode) of the dry powder samples at different annealing stages. (e) XRD patterns of the dry powder samples at different annealing stages.

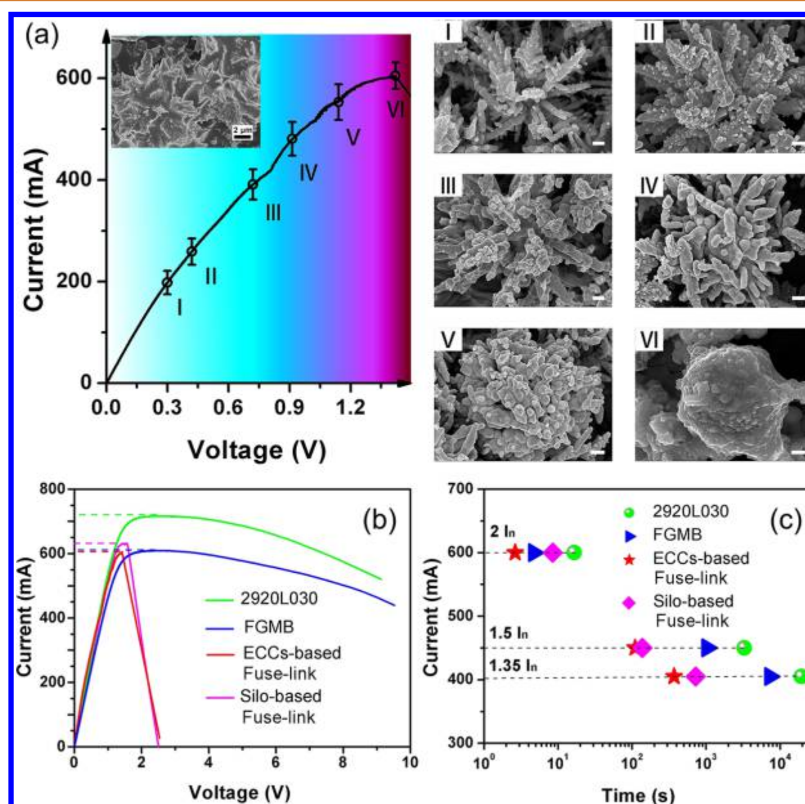

Figure 3. Fusing performance of fuse-links. (a) Various currents on the voltage of the as-prepared ECC-based fuse-link (inset: SEM image of the as-prepared silver paste). The SEM images show the morphology evolution of silver dendrites in ECCs, as the fuse element of fuse-link, during the fusing test (scale bars in I−VI are all 500 nm). (b) Various currents on the voltage during the fusing test of ECC-based fuse-links and commercially available counterparts. (c) Response time of fuse-links at different degrees of overcurrent.

temperature fusing behavior and a high efficiency in breaking the conductive network.

The fusing process can also be monitored *via* observing the optical absorption information on the samples due to the surface plasmon resonance (SPR) characteristic, which can reflect the evolution of both the size and shape of the micro/nanodendrite powder samples in a stable dielectric environment. After a stepwise heating process in a nitrogen atmosphere, the silver micro/nanodendrite samples were analyzed by UV−vis spectroscopy. As shown in Figure 2d,

DOI: 10.1021/acsnano.7b00935
ACS Nano 2017, 11, 7710−7718

the silver micro/nanodendrites exhibited three distinctive absorption bands located at 350, 395, and 450 nm at room temperature, respectively. The absorption peak at 350 nm corresponds to the SPR characteristic of the main body of the silver micro/nanodendrites,[28] and the peak at 395 nm possibly corresponds to the submicrometer-sized secondary branches of silver micro/nanodendrites, which can be attributed to the out-of-plane quadrupole and the out-of-plane dipole resonances,[29] respectively. In addition, the absorption band located at 450 nm could be attributed to the in-plane quadrupole resonance, representing the abundant nanosized tertiary branches at the outermost parts of the silver micro/nanodendrites.[30] With an increase of the treatment temperature, the peak intensity at 450 nm decreased at about 150 °C, corresponding to the melting of nanosized tertiary branches at the outermost parts of the silver micro/nanodendrites (Figure S2b). Then it completely disappeared at 200 °C, while the absorption peak at 395 nm was still obvious, which was attributable to the uneven surface structures of the primary branches (Figure 2b and Figure S2c). As the treatment temperature was raised to 300 °C, the absorption peak at 395 nm decreased significantly, indicating the further diminishing of the surface nanostructures and thus remaining smoother primary branches (Figure S2d). When the treatment temperature further rose to 400 °C, only the peak at 350 nm remained, manifesting the complete disappearance of the fractal structures of silver (Figure S2e). Moreover, the detailed morphology evolution of a virtual branch at different temperature is schematically illustrated in Figure S2f to help make understanding more explicit.

In addition, the X-ray diffraction (XRD) patterns of the silver micro/nanodendrites after being annealed at different temperatures demonstrate the structural evolution and lattice plane transformation during the annealing process. As shown in Figure 2e and Figure S3, with the increase of the treatment temperature, the relative intensity of the diffraction peak of the (111) facet declined gradually; hence the intensity ratio of other diffraction peaks to the (111) peak increased, especially for the (200) peak, which reached 0.42 after annealing at 400 °C, displaying the transformation of crystal planes during the annealing process. Both the morphology and structure of the silver micro/nanodendrites changed significantly during the annealing processes, confirming their special advantages when being used as the fuse element of a fuse-link.

Fusing Performance of the ECC-Based Fuse-Link. The silver micro/nanodendrites were dispersed evenly in the resin matrix (Figure 3a, inset), which endows the ECC with an isotropically electrically conductive property. When an applied current was run through the printed ECCs of the fuse-link, the current−voltage relationship was recorded to manifest the fusing performance of the fuse-link, as shown in Figure 3a. As can be seen, with the increase of applied current, the fuse element underwent three stages. In the first stage (cyan area), the voltage almost linearly increased with the current, indicating an ohmic conductive characteristic. The slightly increased resistance was ascribed to the temperature rise in the fuse element. The second stage (blue area) occurred at about 420 mA, where the resistance decreased first and then continued to increase, which suggests a fusing process of the silver micro/nanodendrites. The third stage (purple area) started at about 600 mA, where the voltage increased remarkably while the current was nearly invariable, suggesting the rapid increase of resistance (Figure S4). After reaching the fusing current (602 mA), the current flow decreased dramatically, demonstrating the disconnection in the fuse element.

On the other hand, the morphological evolution of the silver fillers during the fusing process was also investigated. The dendritic silver fillers underwent negligible morphological change in the first stage (Figure 3a; SEM images I−III, corresponding to currents of 198, 259, and 391 mA, respectively), suggesting normal operation of the fuse-link. In the second stage, the accumulated superabundant heat resulted in the further sintering among the nanotips of silver micro/nanodendrites, causing the fusion and shrinkage of the nano- and submicrostructures (Figure 3a, SEM image IV, 420 mA). At a higher current, the remaining branches of the silver micro/nanodendrites shrank considerably, leading to a loose and porous microspheroidal structure with plentiful irregular submicrometer-sized particles on the surface (Figure 3a, SEM image V, 481 mA). After entering the third stage, the conductive fillers shrank to compact silver spheres, with a significantly decreased volume and a much smoother surface (Figure 3a, SEM image VI, 602 mA). The considerable fusion and shrinkage of the silver micro/nanodendrites rendered the breakdown of the as-established conductive networks, resulting in an increase in resistance value and the ultimate non-conductive paste, which is in perfect accordance with the current−voltage curve.

To further investigate the feasibility of the ECC-based fuse-link for practical applications, the key performance characteristics were evaluated and compared with commercially available fuses. The control samples were the most widely used commercial glass-tube fuse and SMD fuse, with the corresponding models of FGMB (FUJI, Japan) and 2920L030 (Littelfuse, USA). Both of them possess a rated current of 300 mA, the same as our ECC-based fuse-link with a silver content of 30 wt % and electrode distance of 20 μm, termed MWF0.3. As shown in Figure 3b, with the steady increase of applied current, the MWF0.3 broke first at 602 mA, followed closely by the FGMB, with a slightly higher fusing current of 607 mA, whereas the 2920L030 broke when the current rose to 716 mA. The relatively low fusing current of FGMB is due to its high internal resistance (5.63 Ω), as listed in Table 1, which can engender enough Joule heat at a lower current, but it also means higher power loss. The lowest fusing current of MWF0.3 suggests the fastest response to the Joule heat, on account of the ample nano- and submicrometer-sized thermally sensitive structures of the dendritic silver fillers, rather than the metal or alloy wires with much larger feature size. After the fuse-links were blown, the current of MWF0.3 decreased much faster than the control samples, and the residue current was almost negligible, which further confirmed its superior performance characteristic.

Furthermore, the response speed at different levels of overcurrent was studied. As shown in Figure 3c, the response time declined rapidly with the increase of overloaded current, owning to the sharp increase in Joule heat. At the same overloaded current, MWF0.3 broke in the shortest time as compared to the commercial samples. For instance, the response time of MWF0.3 was 110 s at 150% of the rated current ($1.5I_n$), which was only 10.63% and 3.35% of that of FGMB and 2920L030, respectively. Moreover, it took only 2.64 s to break the MWF0.3 at 200% of the rated current ($2I_n$). In summary, the as-prepared MWF0.3 could cut off the electrical circuit more promptly and completely under overloaded conditions, showing great potential in protecting

DOI: 10.1021/acsnano.7b00935
ACS Nano 2017, 11, 7710−7718

Table 1. Performance Comparison between the ECC-Based Fuse-Link and the Commercially Available Fuses

	ECC-based fuse-link	commercial products	
	MWF0.3	FGMB	2920L030
rated current	300 mA	300 mA	300 mA
dimension	2 × 10 mm^2	5.2 × 20 mm^2	7.37 × 5.08 mm^2
fuse element	printed ECC	tin-plated copper	PTC material
fuse element size	60 μm × 30 μm × 10 μm	10 mm × Ⓘ 30 μm	5.3 mm × 2.0 mm × 15 μm
processing method	printing and curing	piece-by-piece wire bonding	tableting and sintering
fusing current	602 mA	607 mA	716 mA
resistance	1.37 Ω	5. 63 Ω	1.93 Ω
surface temperature rise (I_n, 4 h)	25.74 °C	42.63 °C	11.65 °C
voltage drop (I_n, 4 h)	0.41 V	1.69 V	0.58 V
response time ($2I_n$)	2.64 s	4.72 s	16.54 s
resistance variation after thermal shock	−1.85%	0.10%	33.50%
resistance variation after electromigration	6.94%	0.10%	14.30%
resistance variation after thermal−humidity aging	1.69%	0.60%	3.90%
voltage withstanding	200 V	120 V	60 V

overcurrent sensitive component in a broad spectrum of applications, such as integrated circuits, semiconductor rectifier elements, light-emitting diodes, power transistors, and batteries.

Moreover, the reliability of fuse-links was evaluated in accordance with testing methods and parameters described in Table S1. As summarized in Table 1 and Figure S5, the as-prepared ECC-based fuse-link (MWF0.3) has excellent thermal shock resistance (Figure S5a), electromigration resistance (Figure S5b) and humidity resistance (Figure S5d), which are close to those of FGMB and significantly higher than those of 2920L030. Meanwhile, the MWF0.3 is capable of withstanding a higher voltage than the commercially available counterparts (Figure S5c). Additionally, the service reliability of the devices was surveyed, according to UL Standards 248-1 and 248-14, as shown in Figure S6. The as-prepared fuse-links underwent a milder surface temperature rise and voltage drop than the commercially available glass-tube FGMB, especially for the epoxy-resin-based fuse-link (Figure S6a, 16.89 °C lower than FGMB in terms of surface temperature rise and only 24.26% of FGMB in terms of voltage drop), which indicated the steady-state operation of the ECC-based fuse-link. More detailed performance characteristic comparisons are summarized in Table 1, and all the results validate convincingly the superior performance characteristics of the ECC-based fuse-link.

To be noted, the resin matrix for the ECC-based fuse-link is not limited to epoxy resin; for instance, it can be changed into silicone grease, and the corresponding fuse performance is almost the same as the epoxy-based fuse-link, as shown in Figure 3b and c. In this scenario, since silicone grease is a deformable material, the fuse-link becomes a flexible and reworkable component, and the detailed investigation is further demonstrated in Figure 4e and the Supporting Information.

Fuse-Link Prototyping and Evaluation. Taking advantages of printed electronics technology and the prominent low-temperature fusing cutoff characteristic of the micro/nano-dendritic silver fillers, we successfully prototyped three types of fuse-links. As shown in Figure 4a, in view of the prevalently commercially available SMD fuses (Figure S7a), MWFs were developed by directly dispensing/printing the ECCs between the silver-plated copper electrode pairs on a wiring board (Figures S8 and S7c) and subsequent thermal curing processes. To ensure safe and stable work in practical applications, the silver migration of the electrode pairs was tested using the water drop tests, and the silver migration progress was inspected by measuring the variation of current with time under an electrical field strength of 50 V/mm at 25 °C, as shown in Figure S9. The initial time corresponding to the current increase was 605 s for 20 μm, 2090 s for 40 μm, 2885 s for 60 μm, and 3380 s for 80 μm, respectively, indicating high silver migration resistance of the electrode pairs. This can be attributed to the low silver content of the electrodes, resulting in more time to supply enough silver atoms for the growth of Ag dendrites (Figure S9 SEM insets) and formation of a

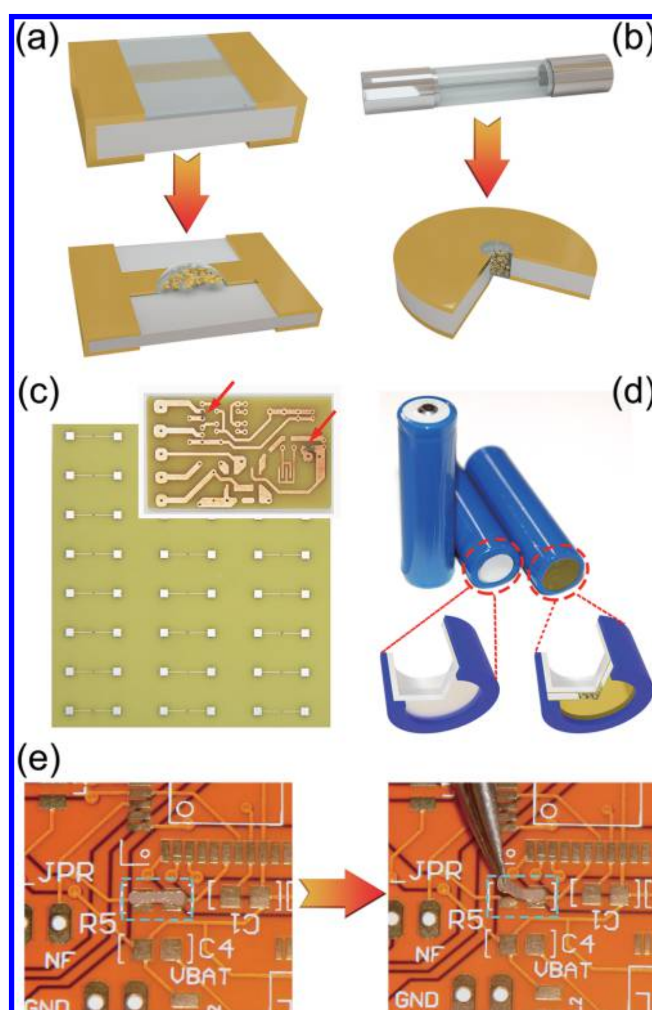

Figure 4. Prototyping of the ECC-based fuse-links. (a) Development of plate fuses: from complex SMD components to a miniaturized wiring-type fuse-link (MWF). (b) Development of cylinder fuses: from a conventional glass-tube fuse to a thin gasket-type fuse-link (TGF). (c) MWF arrays and ECC-based fuse-link on an integrated circuit. (d) TGF packaged directly onto an 18650-type LIB; the corresponding internal structures are diagrammed on the bottom. (e) Silicone-grease-based fuse-link (SGF) was posted on a flexible printed circuit board and then peeled off using a tweezer to replace it.

DOI: 10.1021/acsnano.7b00935
ACS Nano 2017, 11, 7710−7718

conductive network (Figure S9 SEM images). Moreover, the silver migration resistance can be further improved *via* the subsequent packaging.

The fusing current of MWFs is closely related to the resistance value of the fuse element and thus can be conveniently adjusted by regulating the geometric dimension or volume resistivity of the fuse element. Hence, a wide range of fusing currents were obtained by modulating the electrode distance (geometric dimension) and silver content (volume resistivity, Table S2) of the printed ECCs, as listed in Table 2.

Table 2. Fusing Currents of the MWF with Different Electrode Distances and Silver Contents

	electrode distance			
silver content	20 μm	40 μm	60 μm	80 μm
20 wt %	400 mA	350 mA	300 mA	200 mA
	MWF0.2	MWF0.175	MWF0.15	MWF0.1
30 wt %	600 mA	510 mA	430 mA	280 mA
	MWF0.3	MWF0.255	MWF0.215	MWF0.14
40 wt %	770 mA	700 mA	650 mA	570 mA
	MWF0.385	MWF0.35	MWF0.325	MWF0.285

Each fuse was named after the type of fuse-link (*e.g.*, MWF) and the corresponding rated current (*e.g.*, 0.3 for 300 mA). It turned out that a higher fusing current can be obtained at higher conductive filler loading level when the electrode distance was fixed. Likewise, when the silver content was definite, the larger the electrode distance, the lower the fusing current that can be achieved. The fusing current was generally high at the same volume resistivity and geometric dimension (Table S3) when introducing commercial silver flakes as the fillers, which can be attributed to its inferior fuse-blowing ability. When compared with commercial SMD counterparts, the as-prepared MWF0.385 and MWF0.255 showed comparable fusing current levels to the commercial Littelfuse 04670.375 and 04670.25 specimens, respectively. It is noteworthy that the fusing current of MWF could be modulated to as low as 200 mA, which means the corresponding rated current is 100 mA, only 40% of the minimum value of Littelfuse 467 series fuses (250 mA). Since the fusing current depends highly on the silver content and geometric dimension of the printed ECC area, which can be discretionarily adjusted in a wide range, a lower rated current can be easily achieved with a lower silver content or a larger electrode distance. Furthermore, the rheological measurement showed that the complex viscosity of the ECCs increased slightly and then decreased constantly with the increase of shear rates (Figure S10), confirming the shear thinning behaviors and signifying its high processing adaptability; thus MWF arrays with a large area can be obtained by a simple screen-printing process, as shown in Figure 4c, which shows a competitive advantage for mass production.

The superior process adaptability and a broad spectrum of fusing current range give the current technology great potential in addressing some critical challenges in circuit and component protections, such as power batteries. In spite of the high performance, most LIBs suffer from, or are at risk of, battery fire and explosion when the battery is shorted, overcharged, overheated, compressed, or in other abusing cases,[31] which may cause severe safety problems, such as the Samsung Galaxy Note 7 incident recently reported. Currently, safety issues have become a major bottleneck hindering the application of LIBs in many fields. To address this concern, commercial power LIBs are required to be equipped with a battery management system (BMS), Because the integrated circuits in the BMS are vulnerable parts, which are susceptible to electrical overstress, electrostatic discharge issues, *etc.*,[32] a secondary protective element is very essential. According to a survey from Techno Systems Research, the shipment of a secondary protective element for LIBs has exceeded 6 billion pieces in 2015 and is still rising, with an annual growth rate of 10.3%.[33] The main secondary protective elements include positive temperature coefficient (PTC) resistors and thermal fuses.[33,34] A PTC resistor can be reversibly operated, while challenges such as slow response speed, finite breaking current, and considerable leakage current still need to be overcome.[35] Whereas thermal fuses with the advantages of low resistance, fast response speed, precise current/temperature shutdown, and negligible residual current have been increasingly adopted in LIB protection, particularly in large operating current conditions,[33] commercially available thermal fuses for LIB protection (Figure S11) can hardly be assembled into a single battery cell directly due to the size limit and lack of proper packaging technique, which is disadvantageous for complete protection.

Taking the advantage of the outstanding material and the corresponding printing/packaging techniques, we developed a different kind of thin gasket-type fuse-link (Figures S12 and S7d). Experimental observations confirmed that it was a superior alternative for the conventional glass-tube fuse (Figure S7b), for the purpose of single-cell-level protection, as shown in Figure 4b. Likewise, the fusing current of TGF can be adjusted by tuning the parameters of the fuse element, as displayed in Table 3. Besides, the as-prepared TGF has the comprehensive

Table 3. Fusing Currents of the TGF with Different through-Hole Diameters

	diameter			
silver content	0.5 mm	1.0 mm	1.5 mm	2.0 mm
15 wt %	500 mA	1020 mA	1660 mA	2530 mA
	TGF0.25	TGF0.51	TGF0.83	TGF1.265

advantages of wide-range adjustable fusing current, fast response speed, high reliability, and negligible leakage current, coupled with a thin form factor and the ability to be easily batch produced. Moreover, the designed gasket-type configuration enables it to be conveniently attached onto the negative electrode of an 18650 type Li-ion battery, as shown in Figure 4d. Figure S13 further demonstrates the efficient protection function of the as-prepared TGF. The TGF was attached directly onto an 18650 type Li-ion battery, with a fusing current of 1660 mA. Then, it was connected with a single-pole single-throw switch, a slide rheostat, and an ampere meter. In the initial state, the slide rheostat was set to a maximal range (20 Ω), and the corresponding current was around 0.2 A. Then the current was increased gradually by regulating the slide rheostat. When it reached the fusing current, the circuit was completely cut off immediately. The response time was about 0.1 s (Supplementary Video 1), confirming a fast breaking behavior. In practical use, the power batteries are usually packaged into a pack with multiple units. In a battery pack, when one battery is shorted, the other batteries will inevitably charge it, which may trigger a sharp rise in temperature inside the shorted one because of the strong exothermic reaction, resulting in an increased risk of thermal runaway and even catastrophic fire or explosion (Figure S14a). However, provided that each single

DOI: 10.1021/acsnano.7b00935
ACS Nano 2017, 11, 7710−7718

LIB is equipped with a TGF, as illustrated in Figure S14b, the TGF will break to cut off the circuit when the normal batteries discharge to the internal shorted ones, due to the excessive current. Hence, the connection between the shorted batteries and other ones can be efficiently cut off to prevent catastrophic accidents. In brief, the prototyped TGF provides a feasible method to improve the safety performance of LIBs, especially for single unit cell level protection.

Using a composite fusing element also enables us to develop a special kind of deformable and reworkable fuse-link (SGF), by involving the silver micro/nanodendrites fillers and deformable silicone grease dispersant. Hence, it is very convenient to replace it when it is out of operation. As shown in Figure 4e, the dog-bone-shaped miniaturized SGF was directly transferred onto the flexible printed circuit board from the release film like a "Post-it note" and could be peeled off effortlessly using a tweezer when it needed to be replaced. In addition, the excellent deformation ability of the silicone grease enabled the SGF to endure high degrees of deformation along with the flexible printed circuit board (Figure S15). Moreover, the completely severed SGF could be self-repaired with good mechanical property and almost no resistance variation (Figure S16) after only several minutes at room temperature, just like a conductive plasticine, suggesting its excellent ability to self-heal upon encountering damage, as reported in previous work.[36,37] The resistance variation of the SGF after thermal−humidity aging (85 °C, 85% RH, 1000 h) indicated its high reliability (Figure S17), which could be further improved through a subsequent package process. In summary, the as-prepared SGF, with the advantages of easy to batch and liable to install and replace, coupled with deformability, reworkability, and high reliability, shows great potential for applications in future flexible electronic devices.

CONCLUSIONS

In summary, we have demonstrated the feasibility of an ECC-based fuse-link by the introduction of silver micro/nanodendrites and systematically revealed the specific low-temperature fusing and shrinking mechanism due to the dendritic silver filler configuration and the abundant nanosized surface feature. Key performance indicators of the fuse-link are significantly improved, such as lower rated current, shorter response time, and higher working stability and reliability. Moreover, due to the isotropic 3-D geometric characteristic, they are more competitive to render isotropic percolation by printing than other anisotropic micronanostructures,[25] such as 1-D wires[38,39] and 2-D flakes.[40] As illustrated in Figure S18, the shear force during the printing or dispensing process may induce alignment of 1-D wires and 2-D flakes, causing an orientation distribution along with the force direction. Hence, the contact resistance along the filler-aligned direction can be far below the normal direction, which means an anisotropic electrical conductivity. The isotropic 3-D radial configuration of silver micro/nanodendrites can render its homogeneous dispersion in a resin matrix and random distribution during the printing process (Figure S18d), resulting in uniform contact resistance in all directions, namely, isotropic electrical conductivity, which is critical to achieve a high consistency of fusing performance in mass production.

Fusing currents of the ECC-based fuse-link can be precisely modulated in a wide range by adjusting the silver paste and configuration sizes, and even the reproducibility can be regulated by changing the resin matrix. Accordingly, three types of fuse-link configurations were prototyped to address some critical challenges in future diversified electronic devices: (i) the MWF with tiny size, ultralow fusing current was prototyped to protect future higher integration and lower dissipation circuits; (ii) the TGF was designed to be integrated into a single battery cell for safety management; (iii) the deformable and reworkable SGF shows great potential applications in future diversified flexible electronic devices. Compared with traditional fuse-links, the present work makes breakthroughs in fusing mechanism, key materials, component configurational design, and fabrication technique. Furthermore, this work would inspire the development of other printed electronic components to address some critical challenges in future applications, such as resettable circuit breakers or relays, logic switches, and resistance random access memory (RRAM), by virtue of the physicochemical properties of nanomaterial fillers or the distinct nature of the resin matrix.

METHODS

Synthesis and Iodination of Silver Micro/Nanodendrites. The silver micro/nanodendrites were prepared by a multichannel microdroplet reaction.[25] In a typical experiment, 5 mL of silver nitrate aqueous solution (0.06 M, Sinopharm Chemical Reagent Co., Ltd.) was injected into a beaker using a syringe, and then 20 mL of hydroxyl amine aqueous solution (0.48 M, Alfa Aesar) was pumped into the beaker at a velocity of 20 mL·min^{-1} by a multichannel peristaltic pump at room temperature. To mix the droplets homogeneously, the beaker was shaken vigorously during the reaction. Since the silver micro/nanodendrites were obtained merely by the room-temperature reduction of silver nitrate with hydroxyl amine in aqueous solutions, it can be readily scalable to a large amount. We have achieved the controllable synthesis of silver micro/nanodendrites in hundred-gram scale.

The precipitate was washed several times with deionized water and subsequently dispersed in ethanol (99.5%, Sinopharm Chemical Reagent Co., Ltd.) with a magnetic stirrer. Meanwhile, iodine granules (99.5%, Sinopharm Chemical Reagent Co., Ltd.) was dissolved in ethanol to obtain an iodine solution, which was then added dropwise to the stirring silver−ethanol solution to modify the surface of the silver micro/nanodendrites, with an iodine concentration of 8 wt %.[41] Afterward, the treated silver micro/nanodendrites were collected using a simple filtration method and dried in a fume hood. All these processes were operated at ambient temperature.

Preparation of Silver Micro/Nanodendrites-Based ECCs. The epoxy binder was obtained by mixing the bisphenol A-type epoxy (Shell Epon 828, Shell Co., The Netherlands) and methyl tetrahydrophthalic anhydride (Lindau Chemicals Inc., USA) as the curing agent in a mole ratio of 1:1.05 based on the epoxide equivalent weight of the epoxy resin and the hydroxyl equivalent weight of the hardener. A small amount of hexamethylenetetramine (99.5%, Guangzhou Chemical Reagent Factory, China), which acted as a catalyst, was added to the resin dispersant to accelerate cross-linking. Subsequently, the treated silver powders were dispersed in the epoxy binder and were mixed in a planetary rotary mixer (Hasai Co., Shenzhen, China) at 800 rpm for 10 min. The silver contents of the ECCs were controlled to be 15, 20, 30, and 40 wt %, respectively.

For the silicone-grease-based ECCs, the vinyl-terminated polydimethylsiloxane (Shin-Etsu Chemical Corporation, Japan) was mixed with hydroxyl-silicone oil (Shuotai Technology Company, Shenzhen, China) with a mass ratio of 25:1 to form a deformable resin matrix. Tiny amounts of platinum (Shuotai Technology Company, Shenzhen, China) was added to accelerate the curing process. Afterward, the silver micro/nanodendrites were dispersed into the mixture with a filler loading of 50 wt % and further mixed uniformly using the planetary rotary mixer.

Fabrication of Fuse-Links. Three types of fuse-link prototypes were fabricated to cater to different application scenarios, including the

DOI: 10.1021/acsnano.7b00935
ACS Nano 2017, 11, 7710−7718

miniaturized wiring-type fuse-link, thin gasket-type fuse-link, and silicone-grease-based fuse-link.

To protect future higher integration and lower dissipation circuits, the MWF was fabricated by dispensing or printing silver micro/nanodendrites-based ECCs between copper pads, as illustrated in Figure S8. First, the copper electrode pads were fabricated with a copper-clad plate using photolithography. All the copper electrodes shared a width of 30 μm, and the electrode distances were controlled to be 20, 40, 60, and 80 μm, respectively, with a size variation less than 5 μm. Second, the copper pads were treated to prevent oxidation by a chemical silver-plating method. Third, the as-prepared silver micro/nanodendrites-based ECCs with different filler loadings were dispensed in the controlled space between two silver-plated copper electrodes, followed by a heating process at 150 °C for 30 min. Thus, MWF arrays with different sizes and silver contents were obtained.

To solve safety issues in LIBs, the prototyped TGF was fabricated according to the preparation process shown in Figure S12. Before the fabrication process, the PTFE membrane (500 ± 10 μm thick, DuPont Co., Wilmington, DE, USA) and heat-resistant double-sided adhesive tape (with a thickness of 100 μm, 3M 300LSE, 3M Co., USA) was drilled to obtain through-holes with diameters of 0.5, 1, 1.5, and 2 mm, respectively, using a high-speed mini bench drill (LYZ-TZ, Guangzhou, China). After that, it was punched into circular sheets with a diameter of 18 mm and the drilled hole was confined in the middle, using a precision disc cutter (T-06, MTI Corporation, USA). Meanwhile, a copper foil (100 μm thick) was also cut into circular sheets of the same diameter with a laser cutting system (EP-15-DW, Han's Laser Technology Industry Group Co., Ltd., Shenzhen, China).

Then, the TGF was fabricated as follows. First, the circular copper sheet was adhesive-bonded with the drilled circular PTFE membrane using the drilled heat-resistant double-sided adhesive tape, aligned along the drilled holes. Second, the silver micro/nanodendrites-based ECCs with a filler loading of 15 wt % were injected into the holes and precured at 80 °C for 30 min in a vacuum oven. Third, the other circular copper sheet was attached onto the opposite side with the drilled heat-resistant double-sided adhesive tape to constitute an integrated fuse-link. Subsequently, the whole device was heated at 150 °C for 30 min to ensure the ECCs were fully cured.

For the SGF, the silicone-grease-based ECCs were screen-printed onto the release film and then cured at 110 °C for 30 min to form a reworkable and elastomeric fuse-link.

Fusing Performance Test of Fuse-Link. The fusing performance of the above-mentioned three types of ECCs-based fuse-links was investigated with a Solartron 1470E Cell Test System (Solartron Instruments Ltd., UK). Before testing, two silver-plated copper electrodes of the MWF were connected to the positive electrode and negative electrode of the testing system, respectively. Likewise, the fusing performance of the SGF was also tested by dispensing silicone-grease-based ECCs between the silver-plated copper electrodes on an FR-4 board, while the TGF could be directly clamped between the positive and negative electrodes of the electrode holders. Afterward, a direct current was applied to the as-prepared fuse-link, increasing programmatically at a speed of 10 mA/s until the fuse element was fused (Figure S4). The corresponding maximum current was considered as the fusing current.

Characterization of Materials and Devices. The sintering and fusing processes of both the silver micro/nanodendrites and ECCs were observed by a field emission scanning electron microscope (Hitachi S4800, Japan). The crystal structure information on the silver micro/nanodendrites was characterized by powder X-ray diffraction at a scan rate of 10°/min using a Rigaku diffractometer (D/MAX-2500, Japan) equipped with Cu Kα radiation (λ = 1.5418 Å), after heat treatment at different temperatures ranging from room temperature to 400 °C. The light absorption property of the silver micro/nanodendrites at different heat treatment stages was investigated by UV−vis spectroscopy (SCINCO, S-4100, Korea) with an integrating sphere and scanning wavelength from 200 to 1100 nm. Thermal gravitiy−differential scanning calorimetry analysis was conducted on a simultaneous thermal analyzer (NETZSCH SAT 449F3, Germany). The volume resistivities of the ECCs were measured using a four-point probe (MCP-T610, Mitsubishi Chemical Analytech Co. Ltd., Japan) and a resistance meter (RM3545, HIOKI, Japan). The rheological property was tested by a rotational rheometer (MCR302, Anton Paar GmbH, Austria). The currents and voltages of the fuse-links in the fusing process were directly recorded by a cell test system (Solartron 1470E, Solartron Instruments Ltd., UK). The temperature rise was recorded using a data logger (Agilent 34972A, Agilent Technologies, USA). The thermal shock resistance (−65 to 125 °C) was characterized by a thermal shock chamber (TS120, Weiss-Voetsch Environmental Testing Instruments Co., Ltd., Germany). The electromigration property of the fuse-links was studied (85 °C, 85% RH) in a humidity chamber (SETH-A-020R, ESPEC, Japan). The dielectric withstand voltage test was conducted on a programmable withstanding voltage tester (CS2671A, Nanjing Changsheng Instrument Co., China). The thermal−humidity reliability performance of the epoxy-based fuse-link (40 °C, 90% RH) and silicone-grease-based fuse-link (85 °C, 85% RH) was assessed in a humidity chamber (SETH-Z-042L, ESPEC, Japan). The silver migration of the silver-plated copper electrode pairs was tested on the cell test system (Solartron 1470E, Solartron Instruments Ltd., UK) using the water drop tests under an electrical field strength of 50 V/mm at 25 °C.

ASSOCIATED CONTENT

Supporting Information

The Supporting Information is available free of charge on the ACS Publications website at DOI: 10.1021/acsnano.7b00935.

Additional figures (PDF)

Movie demonstrating the TGF protecting a working 18650-type LIB (AVI)

AUTHOR INFORMATION

Corresponding Author

*E-mail: yang.cheng@sz.tsinghua.edu.cn.

ORCID

Yang Wang: 0000-0001-5057-1870

Cheng Yang: 0000-0003-2618-4787

Notes

The authors declare no competing financial interest.

ACKNOWLEDGMENTS

This research was funded by the National Key Basic Research Program of China (Project No. 2014CB932400), the National Nature Science Foundation of China (Project Nos. 51578310 and 51607102), China Postdoctoral Science Foundation (Project Nos. 2016M601017 and 2016M601001), Guangdong Province Science and Technology Department (Project Nos. 2014B090915002, 2014A010105002, and 2015A030306010), and Shenzhen Government (Project No. JCYJ20150518162144944).

REFERENCES

(1) Zhang, L.; Roling, L. T.; Wang, X.; Vara, M.; Chi, M.; Liu, J.; Choi, S.-I.; Park, J.; Herron, J. A.; Xie, Z.; Mavrikakis, M.; Xia, Y. Platinum-Based Nanocages with Subnanometer-Thick Walls and Well-Defined, Controllable Facets. *Science* **2015**, *349*, 412−416.

(2) Pang, X.; He, Y.; Jung, J.; Lin, Z. 1D Nanocrystals with Precisely Controlled Dimensions, Compositions, and Architectures. *Science* **2016**, *353*, 1268−1272.

(3) Tee, B. C.-K.; Chortos, A.; Berndt, A.; Nguyen, A. K.; Tom, A.; McGuire, A.; Lin, Z. C.; Tien, K.; Bae, W.-G.; Wang, H.; Mei, P.; Chou, H.; Cui, B.; Deisseroth, K.; Ng, T. N.; Bao, Z. Skin-Inspired Organic Digital Mechanoreceptor. *Science* **2015**, *350*, 313−316.

(4) Chen, D.; Chen, C.; Baiyee, Z. M.; Shao, Z.; Ciucci, F. Nonstoichiometric Oxides as Low-Cost and Highly-Efficient Oxygen

Reduction/Evolution Catalysts for Low-Temperature Electrochemical Devices. *Chem. Rev.* **2015**, *115*, 9869−9921.
(5) Peng, P.; Hu, A. M.; Gerlich, A. P.; Zou, G. S.; Liu, L.; Zhou, Y. N. Joining of Silver Nanomaterials at Low Temperatures: Processes, Properties, and Applications. *ACS Appl. Mater. Interfaces* **2015**, *7*, 12597−12618.
(6) Campbell, C. T.; Parker, S. C.; Starr, D. E. The Effect of Size-Dependent Nanoparticle Energetics on Catalyst Sintering. *Science* **2002**, *298*, 811−814.
(7) Sivaramakrishnan, S.; Chia, P.-J.; Yeo, Y.-C.; Chua, L.-L.; Ho, P. K.-H. Controlled Insulator-To-Metal Transformation in Printable Polymer Composites with Nanometal Clusters. *Nat. Mater.* **2007**, *6*, 149−155.
(8) Yang, C.; Xie, Y.-T.; Yuen, M. M. F.; Xiong, X.; Wong, C. P. A Facile Chemical Approach for Preparing a SERS Active Silver Substrate. *Phys. Chem. Chem. Phys.* **2010**, *12*, 14459−14461.
(9) Chun, K.-Y.; Oh, Y.; Rho, J.; Ahn, J.-H.; Kim, Y.-J.; Choi, H. R.; Baik, S. Highly Conductive, Printable and Stretchable Composite Films of Carbon Nanotubes and Silver. *Nat. Nanotechnol.* **2010**, *5*, 853−857.
(10) Grouchko, M.; Roitman, P.; Zhu, X.; Popov, I.; Kamyshny, A.; Su, H.; Magdassi, S. Merging of Metal Nanoparticles Driven by Selective Wettability of Silver Nanostructures. *Nat. Commun.* **2014**, *5*, 2994−2998.
(11) Lu, Y.; Huang, J. Y.; Wang, C.; Sun, S.; Lou, J. Cold Welding of Ultrathin Gold Nanowires. *Nat. Nanotechnol.* **2010**, *5*, 218−224.
(12) Garnett, E. C.; Cai, W.; Cha, J. J.; Mahmood, F.; Connor, S. T.; Christoforo, M. G.; Cui, Y.; McGehee, M. D.; Brongersma, M. L. Self-Limited Plasmonic Welding of Silver Nanowire Junctions. *Nat. Mater.* **2012**, *11*, 241−249.
(13) Ahn, J.; Seo, J.-W.; Kim, J. Y.; Lee, J.; Cho, C.; Kang, J.; Choi, S.-Y.; Lee, J.-Y. Self-Supplied Nano-Fusing and Transferring Metal Nanostructures *via* Surface Oxide Reduction. *ACS Appl. Mater. Interfaces* **2016**, *8*, 1112−1119.
(14) Park, S.; Vosguerichian, M.; Bao, Z. A Review of Fabrication and Applications of Carbon Nanotube Film-Based Flexible Electronics. *Nanoscale* **2013**, *5*, 1727−1752.
(15) Tai, Y.-L.; Yang, Z.-G. Fabrication of Paper-Based Conductive Patterns for Flexible Electronics by Direct-Writing. *J. Mater. Chem.* **2011**, *21*, 5938−5943.
(16) Zhu, C.; Du, D.; Eychmüller, A.; Lin, Y. Engineering Ordered and Nonordered Porous Noble Metal Nanostructures: Synthesis, Assembly, and Their Applications in Electrochemistry. *Chem. Rev.* **2015**, *115*, 8896−8943.
(17) Krishna, K. S.; Sandeep, C. S. S.; Philip, R.; Eswaramoorthy, M. Mixing Does the Magic: A Rapid Synthesis of High Surface Area Noble Metal Nanosponges Showing Broadband Nonlinear Optical Response. *ACS Nano* **2010**, *4*, 2681−2688.
(18) Ma, R.; Kang, B.; Cho, S.; Choi, M.; Baik, S. Extraordinarily High Conductivity of Stretchable Fibers of Polyurethane and Silver Nanoflowers. *ACS Nano* **2015**, *9*, 10876−10886.
(19) Chien, C.-C.; Jeng, K.-T. Noble Metal Fuel Cell Catalysts with Nano-Network Structures. *Mater. Chem. Phys.* **2007**, *103*, 400−406.
(20) Fukuda, K.; Someya, T. Recent Progress in the Development of Printed Thin-Film Transistors and Circuits with High-Resolution Printing Technology. *Adv. Mater.* **2017**, *29*, 1602736.
(21) Kelly, A. G.; Hallam, T.; Backes, C.; Harvey, A.; Esmaeily, A. S.; Godwin, I.; Coelho, J.; Nicolosi, V.; Lauth, J.; Kulkarni, A.; Kinge, S.; Siebbeles, L. D. A.; Duesberg, G. S.; Coleman, J. N. All-Printed Thin-Film Transistors from Networks of Liquid-Exfoliated Nanosheets. *Science* **2017**, *356*, 69−73.
(22) Li, Z.; Le, T.; Wu, Z.; Yao, Y.; Li, L.; Tentzeris, M.; Moon, K. S.; Wong, C. P. Rational Design of a Printable, Highly Conductive Silicone-Based Electrically Conductive Adhesive for Stretchable Radio-Frequency Antennas. *Adv. Funct. Mater.* **2015**, *25*, 464−470.
(23) Choi, M. K.; Yang, J.; Kang, K.; Kim, D. C.; Choi, C.; Park, C.; Kim, S. J.; Chae, S. I.; Kim, T.-H.; Kim, J. H.; Hyeon, T.; Kim, D. Wearable Red-Green-Blue Quantum Dot Light-Emitting Diode Array Using High-Resolution Intaglio Transfer Printing. *Nat. Commun.* **2015**, *6*, 7149−7156.
(24) *Circuit Protection Market by Type (Overcurrent Protection, Overvoltage Protection, ESD Protection), Device (Circuit Breakers, Fuses, ESD Protection Devices, Surge Protection Devices), Industry, 32323Geography - Global Forecast to 2022*; Top Market Reports by MarketsandMarkets: Pune, Mah, January 2017.
(25) Yang, C.; Cui, X.; Zhang, Z.; Chiang, S. W.; Lin, W.; Duan, H.; Li, J.; Kang, F.; Wong, C. P. Fractal Dendrite-Based Electrically Conductive Composites for Laser-Scribed Flexible Circuits. *Nat. Commun.* **2015**, *6*, 8150−8159.
(26) Pleşca, A. Numerical Thermal Analysis of Fuses for Power Semiconductors. *Electr. Power Syst. Res.* **2012**, *83*, 144−150.
(27) Torres, E.; Mazón, A. J.; Fernández, E.; Zamora, I.; Pérez, J. C. Thermal Performance of Back-Up Current-Limiting Fuses. *Electr. Power Syst. Res.* **2010**, *80*, 1469−1476.
(28) Sun, Y.; Gates, B.; Mayers, B.; Xia, Y. Crystalline Silver Nanowires by Soft Solution Processing. *Nano Lett.* **2002**, *2*, 165−168.
(29) Jin, R.; Cao, Y. C.; Hao, E.; Métraux, G. S.; Schatz, G. C.; Mirkin, C. A. Controlling Anisotropic Nanoparticle Growth through Plasmon Excitation. *Nature* **2003**, *425*, 487−490.
(30) Xia, X.; Zeng, J.; Oetjen, L. K.; Li, Q.; Xia, Y. Quantitative Analysis of the Role Played by Poly (Vinylpyrrolidone) in Seed-Mediated Growth of Ag Nanocrystals. *J. Am. Chem. Soc.* **2012**, *134*, 1793−1801.
(31) Finegan, D. P.; Scheel, M.; Robinson, J. B.; Tjaden, B.; Hunt, I.; Mason, T. J.; Millichamp, J.; Di Michiel, M.; Offer, G. J.; Hinds, G.; Brett, D.; Shearing, P. R. In-Operando High-Speed Tomography of Lithium-Ion Batteries during Thermal Runaway. *Nat. Commun.* **2015**, *6*, 6924−6933.
(32) Voldman, S. H. In *Electrical Overstress (EOS): Devices, Circuits and Systems*; Voldman, S. H., Ed.; ESD Series; John Wiley & Sons Ltd.: Chichester, West Sussex, 2013.
(33) *LIB Material Market Analysis*, 2016 ed.; Marketing Report by Techno Systems Research Co., Ltd.: Chiyoda-ku, TKY, August 2016.
(34) Feng, X. M.; Ai, X. P.; Yang, H. X. A Positive-Temperature-Coefficient Electrode with Thermal Cut-off Mechanism for Use in Rechargeable Lithium Batteries. *Electrochem. Commun.* **2004**, *6*, 1021−1024.
(35) Li, J.; Chen, J.; Lu, H.; Jia, M.; Jiang, L.; Lai, Y.; Zhang, Z. A Positive-Temperature-Coefficient Layer Based on Ni-Mixed Poly (Vinylidene Fluoride) Composites for $LiFePO_4$ Electrode. *Int. J. Electrochem. Sci.* **2013**, *8*, 5223−5231.
(36) Zhang, P.; Li, G. Advances in Healing-on-Demand Polymers and Polymer Composites. *Prog. Polym. Sci.* **2016**, *57*, 32−63.
(37) Jia, X.-Y.; Mei, J.-F.; Lai, J.-C.; Li, C.-H.; You, X.-Z. A Self-Healing PDMS Polymer with Solvatochromic Properties. *Chem. Commun.* **2015**, *51*, 8928−8930.
(38) Xu, Y.; Galderon-Ortiz, G.; Exarhos, A.; Alsayed, A.; Winey, K.; Kikkawa, J.; Yodh, A. *Electrical Anisotropy in Coatings of Aligned Silver Nanowires*, Bulletin of the American Physical Society, APS March Meeting 2015, San Antonio, TX, Mar 2−6, 2015; American Physical Society: Ridge, NY, 2015.
(39) Lanticse, L. J.; Tanabe, Y.; Matsui, K.; Kaburagi, Y.; Suda, K.; Hoteida, M.; Endo, M.; Yasuda, E. Shear-Induced Preferential Alignment of Carbon Nanotubes Resulted in Anisotropic Electrical Conductivity of Polymer Composites. *Carbon* **2006**, *44*, 3078−3086.
(40) Inoue, M.; Muta, H.; Maekawa, T.; Yamanaka, S.; Suganuma, K. Temperature Dependence of Electrical and Thermal Conductivities of an Epoxy-Based Isotropic Conductive Adhesive. *J. Electron. Mater.* **2008**, *37*, 462−468.
(41) Yang, C.; Xie, Y.-T.; Yuen, M. M.-F.; Xu, B.; Gao, B.; Xiong, X.; Wong, C. P. Silver Surface Iodination for Enhancing the Conductivity of Conductive Composites. *Adv. Funct. Mater.* **2010**, *20*, 2580−2587.

DOI: 10.1021/acsnano.7b00935
ACS Nano 2017, 11, 7710−7718